



# Stellar Migration in Galaxy Disks Using the Chirikov Diffusion Rate

Hervé Wozniak 

LUPM, Univ Montpellier, CNRS, Montpellier, France; [herve.wozniak@umontpellier.fr](mailto:herve.wozniak@umontpellier.fr)

Received 2019 August 28; revised 2019 December 2; accepted 2019 December 5; published 2020 January 28

## Abstract

We are reexamining the problem of stellar migration in disk galaxies from a diffusion perspective. We use for the first time the formulation of the diffusion rates introduced by Chirikov, applied to both energy,  $E$ , and angular momentum,  $L_z$ , in self-consistent  $N$ -body experiments. We limit our study to the evolution of stellar disks well after the formation of the bar, in a regime of adiabatic evolution. We show that distribution functions of Chirikov diffusion rates have similar shapes, regardless of the simulations, but different slopes for energy and angular momentum. Distribution functions of derived diffusion timescales,  $T_D$ , also have the same form for all simulations, but are different for  $T_D(E)$  and  $T_D(L_z)$ . Diffusion timescales are strongly dependent on  $L_z$ :  $T_D(E) \lesssim 1$  Gyr in a  $L_z$  range roughly delimited by the set of stellar bar resonances (between the ultraharmonic resonance and the outer Lindblad resonance). Only particles with low  $L_z$  have  $T_D(L_z) \lesssim 10$  Gyr, i.e., the simulation length. In terms of mass fraction, 35%–42% turn out to diffuse energy in a characteristic timescale shorter than 10 Gyr, i.e., simulation length, while 60%–64% undergo the diffusion of the angular momentum on the same timescale. Both the diffusion of  $L_z$  and  $E$  are important to grasp the full characterization of the radial migration process, and we show that depending on the spatial region considered, one or the other diffusion dominates.

*Unified Astronomy Thesaurus concepts:* Galactic and extragalactic astronomy (563); Galaxy dynamics (591); N-body simulations (1083); Galaxy stellar disks (1594); Barred spiral galaxies (136); Dynamical evolution (421); Galaxy evolution (594)

## 1. Introduction

Stellar migration of the galactic disk stars has been invoked as a dynamical mechanism to explain the dispersion of stellar metallicity observed in the solar neighborhood. The age–metallicity relation (AMR) shows that the dispersion of stellar metallicity increases with the age of the stars (e.g., Edvardsson et al. 1993; Haywood 2008; Soubiran et al. 2008; Buder et al. 2019). Another relation, the age–velocity dispersion relation (AVR; e.g., Wielen 1977; Soubiran et al. 2008; Mackereth et al. 2019) suggests the existence of a heating mechanism of the stellar disk. Stellar migration could then also be a cause, although other mechanisms have been proposed.

However, stellar migration does not take place in a hypothetical perfectly axisymmetric disk, made of stars rotating in circular orbits. One or more gravitational perturbations are at the origin of any deviation from this hypothetical perfection. These perturbations can be intrinsic (density waves, such as bars or spiral arms, two-body relaxation, etc.) or extrinsic (galaxy satellites, encounters, mergers, gas accretion, etc.). Also, the amplitude of the perturbations, and thus their ability to reproduce observations, depends on the underlying physical mechanism invoked.

Two classes of models have recently been proposed; they have been the focus of attention since. All of them distinguish between the effects of blurring (i.e., the radial migration of a star is due to epicyclic motion around a fixed guiding radius) and churning (i.e., the radial migration is due to a change in this guiding radius).

Sellwood & Binney (2002) have shown that spiral waves, possibly transient, have the ability to modify the angular momentum of stars without changing the distribution function, so that the disk does not heat up as a result of these changes. These angular momentum changes essentially result in a variation in the mean radius of stellar orbits over time, while

keeping their low eccentricity. The dominant mechanism is thus churning. These spiral waves have their own pattern speeds with which stars may resonate. Sellwood & Binney (2002), confirmed by Roškar et al. (2012), have shown that angular momentum exchanges take place mainly at corotation. Therefore, the corotation scattering mechanism might be responsible for stellar migration.

For Minchev & Famaey (2010), resonances are also responsible for stellar migration, but their mechanism differs somewhat from Roškar et al. (2012). Indeed, Minchev & Famaey (2010), confirmed by Minchev et al. (2011), consider the interactions between a stellar bar and a spiral structure. In this case, at least two patterns exist and the resonances may overlap. Resonance overlap introduces additional chaos by increasing the efficiency of orbit scattering, which also modifies the angular momentum of stars. Indeed, motion in chaotic regions can be diffusive (e.g., Contopoulos 1983a).

We are therefore faced with two mechanisms, which are not irreconcilable from the point of view of galactic dynamics, but which have different observational consequences on the AMR and AVR. Indeed, a related important question for the AVR is whether these phenomena cause just the right amount of chaos in the disk to explain increases in the velocity dispersion over time. Whether we deal with stellar migration, disk heating, or stochasticity, stellar motions can be studied from different viewpoints. Indeed, each analysis uses a different methodological framework, but the fundamental observational fact is that stars do not stay at their birth site. Therefore, the fundamental question, which is still under debate, is not ultimately to know which dynamical process is solely responsible for the radial migration of stars, but rather what are the relative intensities of each of these processes, whether they contribute together to the same phenomenon, or whether they are ultimately only different points of view of the same phenomenon whose root cause should still be determined.

We have decided to tackle the problem with tools of nonlinear physics. This article is only a preliminary step toward answering the fundamental questions mentioned above. Our approach here is to reanalyze the *diffusion* of quantities such as energy and angular momentum. We have measured diffusion by applying for the first time the Chirikov diffusion coefficient to galactic  $N$ -body simulations. Brunetti et al. (2011) have already addressed the issue but in the general context of Fokker–Planck diffusion.

After some fundamental considerations on the dynamics of a rotating disk subjected to perturbations (Section 2), we introduce the Chirikov diffusion rate in Section 3, then  $N$ -body simulations on which we have applied this tool (Section 4). Sections 5 and 6 are dedicated to the analysis of the results that will be discussed in Section 8. Section 7 focuses on an axisymmetric case for the sake of comparison.

## 2. Angular Momentum and Energy Variations

The dynamics of a rotating stellar disk forced by a spiral or a bar (or any other driving force) is well known, and we are reminded by Sellwood & Binney (2002) in the context of stellar migration. For any galactic dynamical system subjected to one perturbative frequency, the only integral of motion is Jacobi’s integral defined as

$$E_J = E - \Omega_p L_z, \quad (1)$$

where  $E$  is the classical energy in the nonrotating inertial frame,  $L_z$  is the angular momentum component on the  $z$ -axis  $\mathbf{e}_z$  chosen to be conveniently the rotation axis, and assuming that  $\Omega = \Omega_p \mathbf{e}_z$ , the frequency of the perturbation.  $E$  is the sum of the kinetic and potential energy in a closed system. Therefore, as  $\Delta E_J \equiv 0$ , any variation of  $E$  is linearly related to  $L_z$  and vice versa as  $\Delta E = \Omega_p \Delta L_z$ .

From the point of view of Hamiltonian dynamics, the existence of two pattern speeds in a galactic disk is similar to a physical system with motions on two different timescales: the so-called slow–fast systems. The fast system could be the bar which has the greater pattern speed whereas a spiral structure could be the slow one. The same situation occurs with the phenomenon of the bar-in-the-bar (Wozniak 2015). For such systems, adiabatic invariants are important dynamical quantities as approximate integral of motion: on the one hand, the motion over long time ranges is almost regular if several such adiabatic invariants exist. On the other hand, dissolution of these invariants is one possible mechanism for onset of chaotic dynamics. Indeed, resonant phenomena in fast motion lead generally to dynamical chaos and transport in large regions of the phase space as they destroy adiabatic invariance.

If several patterns coexist in the disk, each one being possibly variable, the  $\Delta E$  versus  $\Delta L_z$  plane must exhibit several coexisting slopes. This is what simulations of Section 4 would suggest. Indeed, Figure 1 shows that other patterns exist. Therefore, not all mass transfers have the stellar bar as the responsible party. This figure shows also that there is a continuum of  $\Delta E$  and  $\Delta L_z$  values for which mass transfers occurs.

In fact, working with the ratio  $\Delta E/\Delta L_z$  (as Sellwood & Binney 2002 and Roškar et al. 2012 did) masks too much the complexity of the redistribution in  $E$  and  $L_z$ , as this technique focuses on the dominant patterns, whether they are due to the bar or the spiral structures. Alternatively, the study of

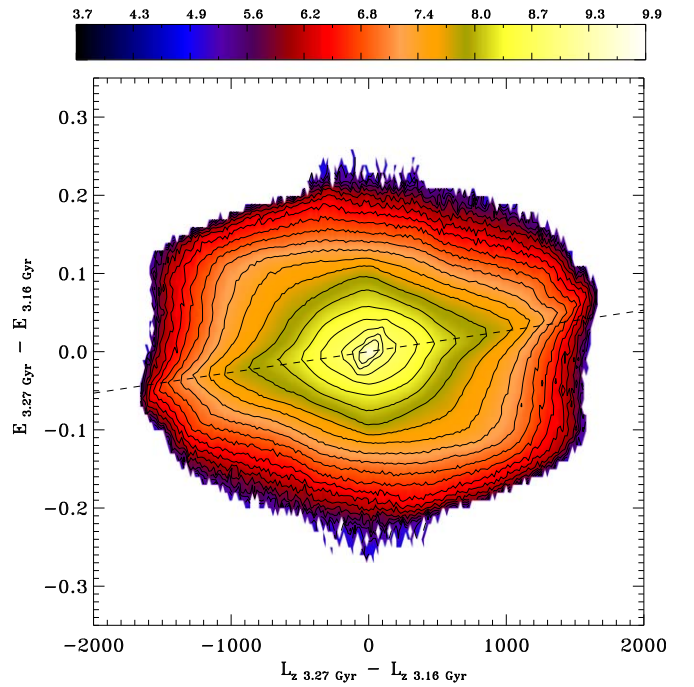


**Figure 1.** Mass distribution in the plane  $\Delta E$  vs.  $\Delta L_z$  for RunC (see Section 4) between times  $t = 3.16$  and  $t = 3.27$  Gyr. The color bar is scaled in  $\log(M_\odot)$  per bin. The dashed line is the location of  $\Delta E = \Omega_p \Delta L_z$ , where  $\Omega_p$  is the bar pattern speed.

variations in  $E$  and  $L_z$  can be based on the difference of these quantities between two times. These times can be distant: this is the case between final and initial values, the notion of “final” being understood here as representative of a typical state of the galaxy. This approach was adopted by all stellar migration studies since Sellwood & Binney (2002), but only for  $L_z$ , with  $\Delta L_z = L_z(t) - L_z(0)$ .

$\Delta L_z(\Delta t) = L_z(t_2) - L_z(t_1)$  is another approach used, for instance, by Roškar et al. (2012). It has the merit of focusing on the relative variations with respect to an earlier time, whatever the meaning to be given at that time. The two times can be close, and as close as we want, so that the difference tends toward a differential. If the study is limited to the consequences of the development of certain structures (e.g., stellar bar, spiral arms), the initial state can be chosen wisely to isolate the perturbation created by these structures. Finally, pushed at infinitely small time intervals, this formulation expresses an instantaneous variation of the angular momentum  $L_z$ , which is related to the net torque acting on the system of particles.

It should be recalled that, at the level of individual particles, taking a particular time as a reference situation is not necessarily more correct than taking the initial time. Indeed, because of the combined effect of relaxation and bar formation, instantaneous individual angular momenta may not be representative of time-averaged angular momenta. For instance, if a particle is able to move *alternatively* outward and inward in radius while preserving the circularity of its orbit (what is typical of an epicyclic orbit with low  $\kappa$  frequency), it contributes to the instantaneous  $\Delta L_z$  taken at any particular time. But averaged on several rotations, the time-averaged  $\overline{L_z}$  is only representative of the mean radius, thus  $\Delta \overline{L_z} \sim 0$ . On the contrary, if that particle moves adiabatically outward or inward exclusively, then  $\Delta \overline{L_z} \neq 0$ . The particle then moves to a

nearby region of the phase space, its mean radius and/or rotational velocity having been modified. There is diffusion.

It is therefore necessary to average the measurements in one way or another, both on the angular momentum and the energy of individual particles. The averaging is intended to cancel the influence of bounded energy/angular momentum oscillations and emphasize the accumulating changes, related to the diffusion process.

### 3. Introduction to Chirikov Diffusion Rate

The diffusion of  $E$  means that the energy of the body, as a result of the accumulation of small random variations, can take larger as well as smaller values, as compared with the unperturbed energy. Similarly, diffusion of  $L_z$  means that even if the trajectory of unperturbed motion of the body was close to circular, a perturbation may bring about trajectories with high eccentricity. If  $E$  increases at constant rotational velocity, it will necessarily generate an increase in  $L_z$ , because the radius increases. However, a similar effect can be achieved by increasing the velocity. Because positions and velocities vary together, the real diffusion rate depends on both  $E$  and  $L_z$ .

In this context, the *Chirikov diffusion rate* (Chirikov 1979, Equation (4.6)) appears to be a natural choice. Applied on  $E$ , for individual particles, it is defined as

$$D_n(E) = \overline{(\Delta E)^2} / \Delta t. \quad (2)$$

Although the original definition deals only with  $E$ , we may extend the definition of Equation (2) to compute  $D_n(L_z)$ . In Equation (2),  $\bar{E}$  is the value of energy averaged over a period of  $\Delta t_n = 10^n$  (in time unit of the system). In our case, it is convenient to choose  $\Delta t_n \equiv \Delta t_2$  as the minimum time that separates two snapshots, i.e., 100 code units (105.49 Myr). Indeed, the whole simulation (10.54 Gyr) is naturally segmented at regular intervals.  $\bar{E}$  and  $\bar{L}_z$  are thus computed on the fly for each particles and stored with snapshots.

$\Delta \bar{E}$  is then the difference between two intervals (snapshots),  $\Delta t$  being the time difference between the snapshots. These snapshots are not necessarily consecutive, as the second averaging concerns all possible pair combinations. This procedure, initiated by Chirikov (1979), ensures that all timescales are represented by the definition of  $D_n$ .

Several other definitions of  $D_n$  exist, and an abundance of the literature concerns the interpretation to be given to the evolution of  $D_n$  with the *strength* of the perturbation(s), and its asymptotic behavior when  $n$  increases (Lichtenberg & Leiberman 1992). As a general rule,  $D_n$  sharply increases above a certain threshold of perturbation strength meaning that the motion is moving from regular to chaotic. We are not looking here for any critical value of the perturbation strength, as the definition of this strength can be the subject of much debate. Indeed, each region of a galactic disk is subjected to perturbations of different intensities while all these regions remain connected through gravitation. It is therefore very difficult to highlight particular threshold values of the perturbation intensity in a large  $N$ -body system, considered as a whole. Our objective is rather to qualify the different types of particle populations with noticeable  $D_n$  values, or range of  $D_n$ , possibly different from one region to another. This allows to determine whether some regions are more stochastic than others and, if so, whether  $E$  or  $L_z$  is the more diffusive quantity.

**Table 1**  
Main Initial Parameters

Model	$N_s$ $\times 10^7$	$M_1$ $\times 10^{10} M_\odot$	$M_2$ $\times 10^{10} M_\odot$	$l_1$ (kpc)	$l_2$ (kpc)	$h_z$ (kpc)
RunA	4.0	0.63	3.57	0.57	2.0	0.5
RunB	4.4	1.1	11.0	1.0	3.5	0.5
RunC	4.0	3.0	17.0	1.14	4.0	1.0

**Note.** Name of the run (Model), number of stellar ( $N_s$ ) particles, masses, scale lengths, and common scale height of the two Miyamoto–Nagai initial distributions ( $M_1, M_2, l_1 = a_1 + h_z, l_2 = a_2 + h_z, h_z$ ).

### 4. $N$ -body Experiments

Several simulations have been performed to check the dependence of our results on certain quantities, such as the total mass, or the initial scale of the stellar disk. Rather than starting from a cosmological situation, including all kinds of effects that are difficult to control (accretion of dwarf galaxies, cold gas flows, star formation, etc.), we preferred to start with an idealized situation.

Initial stellar populations are set up to reproduce such idealized, but typical, disk galaxies. Positions and velocities for  $N_s$  particles are drawn from a superposition of two axisymmetrical Miyamoto & Nagai (1975) disks of mass  $M_1$  and  $M_2$  (see Table 1), of scale lengths  $l_1$  and  $l_2$  kpc and a scale height  $h_z$ . Initial positions have been truncated to  $R = 30$  kpc for RunA and RunB,  $R = 40$  kpc for the more massive RunC. Scale lengths and scale heights have been chosen such as the superposition of the two axisymmetric distributions shapes the initial spatial configuration as a disk galaxy with a small but significant bulge.

Initial velocity dispersions are computed solving numerically the Jeans equations according to the Hernquist (1993) method. The initial velocity dispersion was chosen to be anisotropic with  $\sigma_r = \sigma_z$  and  $\sigma_\theta^2 = \sigma_r^2 \kappa^2 / (4\Omega^2)$ , where  $\sigma_r, \sigma_\theta$ , and  $\sigma_z$  are three components of the velocity dispersion along respectively the radial, azimuthal, and vertical directions and  $\kappa$  and  $\Omega$  are, respectively, the radial and angular epicyclic frequencies. They are related by  $\kappa^2 = 4\Omega^2 + rd\Omega^2/dr$ .

As the Toomre parameter ( $Q = \sigma_r \kappa / (3.36G\mu)$ , where  $\mu$  is the mass surface density, and  $G$  the gravitational constant) has not been explicitly constrained, the resulting values are displayed in Figure 2. The three simulations are unstable ( $Q < 1$ ) in their central region, i.e., at roughly one scale length around the center. This is typically the region where the bar is formed.

RunC and RunA use similar initial parameters than respectively Pfenniger & Friedli (1991) and Brunetti et al. (2011). RunB has similar initial conditions than the run named “SimS” in Wozniak (2015), but is made exclusively of stellar particles for the same total mass. All runs are computed until 10.54 Gyr.

The evolution is computed with a particle-mesh  $N$ -body code, derived from the original version of the Geneva group (Pfenniger & Friedli 1993). The broad outline of the code is as follows. The gravitational forces are computed with a particle-mesh method using a 3D log-polar grid with  $(N_R, N_\phi, N_Z) = (60, 64, 312)$  active cells. The smallest radial cell in the central region is 36 pc large, and the vertical sampling is 50 pc. The extent of the mesh is 100 kpc in radius and  $\pm 7.8$  kpc in height. Because we used a polar grid and we need an accurate

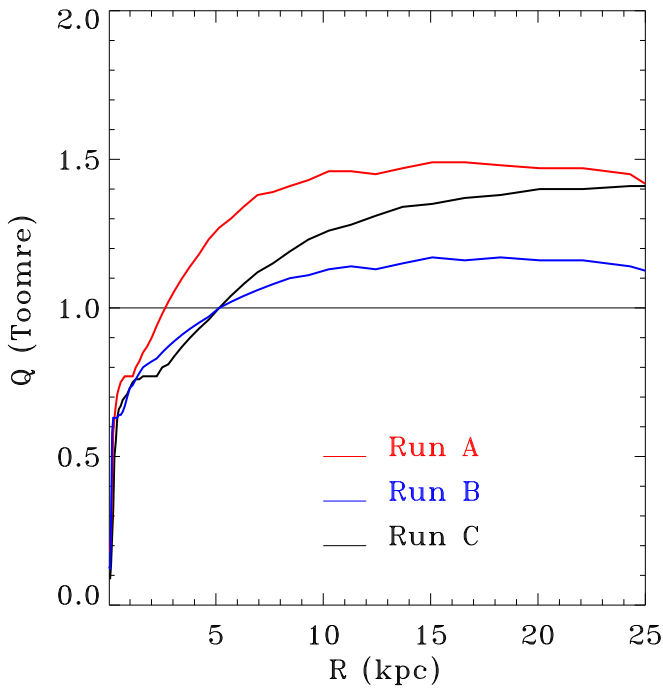


**Figure 2.** Initial  $Q$  Toomre parameter as a function of radius for the three simulations.

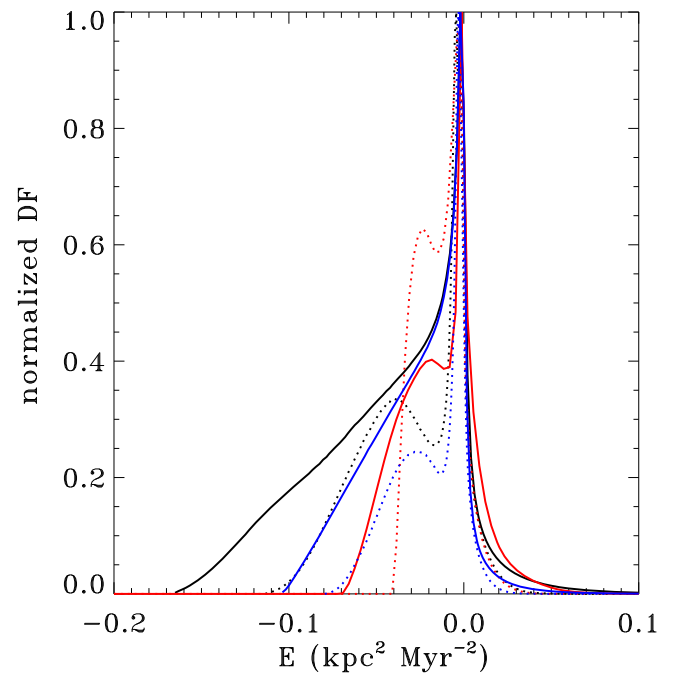
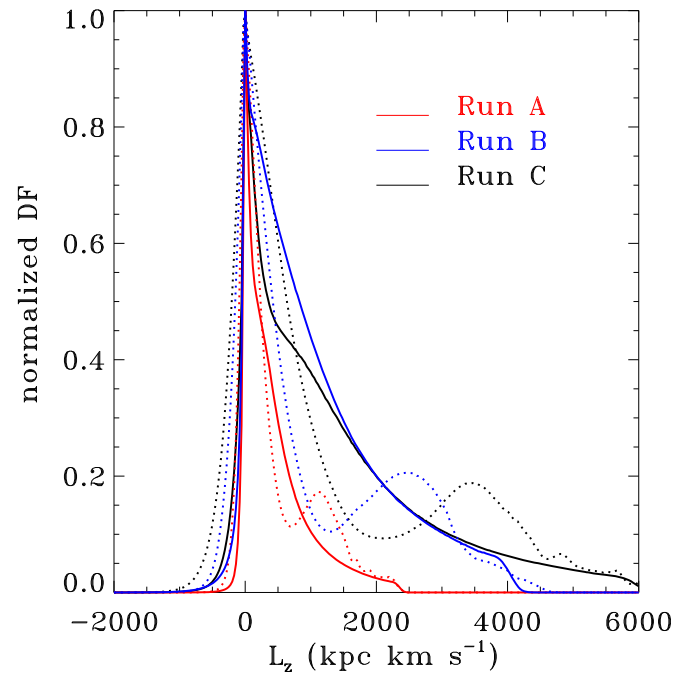
determination of the forces in the central region, we have improved the precomputation of self forces by subdividing each cell in  $(n_r, n_\phi, n_z) = (32, 6, 6)$  subcells. Self forces are then linearly interpolated before being subtracted from the gravitational forces.

In a perfectly collisionless simulation of a stable equilibrium model, each particle would conserve its specific energy. The combination of a particle-mesh code, an initial relaxed distribution, and a large number of particles ensures that the sources of numerical diffusion are minimized. However, we have also performed a control run (RunC<sup>ax1</sup>), which will be detailed in Section 7.

For convenience, the units in which the discussion will be conducted have been chosen to avoid the power of 10. Thus, the specific angular momenta will be in  $\text{kpc km s}^{-1}$ , while the specific total energies will be in  $\text{kpc}^2 \text{Myr}^{-2}$ . In addition, as all particles have the same mass, all particle number distributions can also be read as mass fractions.

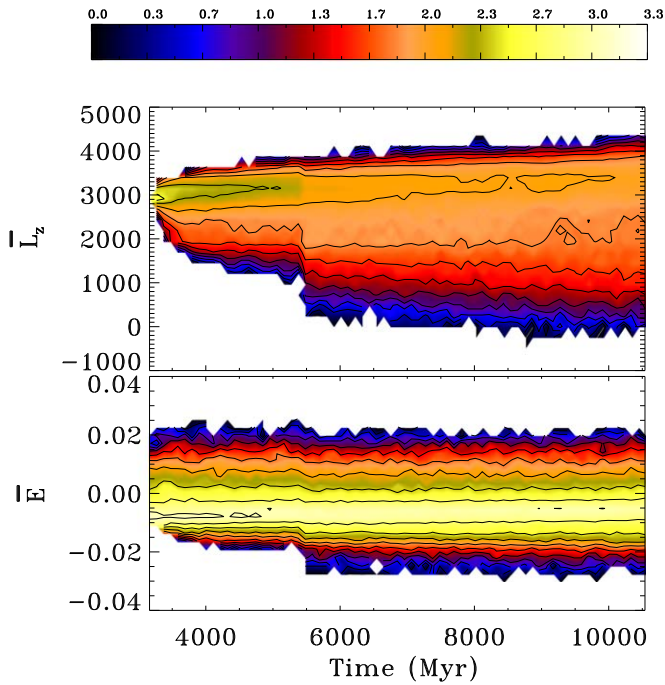
The initial and final distribution functions (DF; see Figure 3) are typical of such type of simulation. Expressed as a function of  $L_z$ , these DF display similar trends in regard to the DF obtained by 3D  $N$ -body simulations, e.g., those of Zang & Hohl (1978), Sparke & Sellwood (1987) or Pfenniger & Friedli (1993). The shape of these DFs has been explained by a superposition of various families of orbits (Wozniak & Pfenniger 1997, 1999). Orbits of the bump (around  $L_z \approx 1100, 2500$  and  $3500 \text{ kpc km s}^{-1}$  for, respectively, RunA, RunB, and RunC) are mostly disk orbits that also populate the corotation region of the bar. These orbits spend most of their time outside the bar and sometimes enter inside the bar from the  $L_{1,2}$  Lagrangian points. This last kind of orbits as well as Lagrangian orbits form the “hot” population described first by Sparke & Sellwood (1987). This “hot” population may contribute up to 30% of the total mass.

Figure 4 displays the evolution of  $\overline{L}_z$  and  $\overline{E}$ , for a group of particles selected for RunC at  $t = 3.27 \text{ Gyr}$  with



**Figure 3.** Initial (solid lines) and final (dotted lines) distribution functions (DF) for the three simulations. DFs have been normalized to DF(0) which is also the maximum. The bump in the final DF, around  $L_z \approx 1100, 2500$  and  $3500 \text{ kpc km s}^{-1}$  for, respectively, RunA, RunB, and RunC, is typical of the “hot” particle population which is able to cross the corotation and explore both the bar and the disk.

$\overline{L}_z = 3000 \pm 0.3 \text{ kpc km s}^{-1}$ , typical of the “hot” population. This selection represents 3847 particles. Although these particles are selected over a narrow interval in  $\overline{L}_z$ , the values of  $\overline{E}$  show initially a larger amplitude, the maximum being around  $-0.0075 \text{ kpc}^2 \text{Myr}^{-2}$ . As the group evolves, the amplitude of  $\overline{L}_z$  increases rapidly, until it reaches a range of values from  $\approx 0$  (or even negative for some particles) to  $\approx 4500$ . The  $\overline{L}_z$  distribution mode increases until it reaches a value of



**Figure 4.** Evolution of  $\overline{L}_z$  (top) and  $\overline{E}$  (bottom), for 3847 particles selected for RunC (see Section 4 for details) at  $t = 3.27$  Gyr with  $\overline{L}_z = 3000 \pm 0.3$  kpc km s $^{-1}$ . The color bar is scaled in  $\log(M_\odot)$  per bin.

$\approx 3500$  at  $t = 10.54$  Gyr. Values of  $\overline{E}$  also vary over the same time interval. However, its distribution gradually spreads only on the negative side. Let us recall here that these are average values over an interval of  $\Delta t_2 = 105$  Myr, i.e., between an half and a quarter of the bar rotation period. Averaging over a larger  $\Delta t_n$  does not change the result.

By looking for potential differences between these simulations, we can focus on power spectra of the  $m = 2$  frequencies between  $t = 2.11$  and  $10.54$  Gyr for RunA and RunB and between  $t = 3.16$  and  $t = 10.54$  Gyr for RunC (see Section 5 for explanation of these time ranges). In Figure 5, the bar frequency largely dominates. Several other patterns exist and give rise to overlaps of resonances. These overlaps are usually temporary because the resonance system linked to the bar slides outwards during the evolution of the disk and the slowing down of the bar. Moreover, as the time window is wide, only long-lived structures appear in this figure. Transient structures, often with a lifetime of less than one orbital period, are erased. However, their role is essential. In a future article, I will analyze more closely their connections with more permanent structures.

### 5. Chirikov Diffusion Rate in $N$ -body Experiments

As  $D_2(E)$  and  $D_2(L_z)$  sum up all fluctuations occurring in the disk, we have intentionally restricted the time interval to the epoch well after the bar formation. Therefore, the computation of  $D_2(E)$  was performed between  $t = 3.16$  and  $t = 10.54$  Gyr for RunC (i.e., 70 snapshots) and between  $t = 2.11$  and  $10.54$  Gyr for RunA and RunB (i.e., 80 snapshots), spaced by  $\Delta t_2$ , i.e., on, respectively, 2415 and 3160 unique pairs. The starting times have been chosen to avoid the strong perturbations caused by the formation of the bar, which are not of interest to us here. This rules out the strong redistribution in  $E$  and  $L_z$  made by the formation of the bar. Doing so, we can

examine the impact of driving forces in a quieter phase of the galaxy.

Although particles escaping the grid are tracked throughout their trajectory by a ballistic approximation, we chose to exclude them from our analyses as soon as they came out of even one time step. This drastic procedure ensures that we limit numerical errors to their lowest values.

Figure 6 shows the distributions for  $D_2(E)$  and  $D_2(L_z)$  for the three simulations. A first lesson that can be drawn from these figures is the universality of the distributions shape when  $D_2$  is normalized to its maximum. Approximatively,

$$\log n(D_2) \propto \gamma D_2 / \max(D_2)$$

where  $\gamma$  is different for  $D_2(E)$  and  $D_2(L_z)$ , and  $n(D_2)$  is the fraction of particles number or, equivalently, the mass fraction.  $\gamma$  is close to  $-5.0$  for  $D_2(E)$  and between  $-6.28$  and  $-6.79$  for  $D_2(L_z)$ . The shape is represented by a linear regression valid over a wider range of  $D_2/\max(D_2)$  for  $L_z$  than for  $E$ .

Deviations from a linear fit are also instructive. For  $D_2(E)$ , two regions deserve to be commented on. The three distributions show a dip for  $D_2(E)/\max(D_2(E)) < 0.04 - 0.06$ . It accounts for a maximum of 30% of the total mass. The second region is at the opposite: the distribution drops when  $D_2(E)$  reach  $\approx 80\%$  of the maximum.

However, the normalization by  $\max(D_2)$ , which allows to compare the profiles between them, masks an important element. Indeed, these maxima are different from one simulation to another in a sensitive way, because they approximately scale with the square of the total energy or angular momentum. Table 2 gives the values of these maxima.

### 6. Diffusion Timescales

The interpretation of  $D_2(E)$  may seem complicated because this quantity mixes information on the quadratic evolution of the  $E$  fluctuations at different timescales. Large fluctuations of  $E$  over long times can contribute as much as small fluctuations over very short times. Formally, we can also estimate a diffusion timescale  $T_D$  by renormalizing  $D_n$  by  $E^2$  and  $L_z^2$ , respectively. As Chirikov diffusion rate takes care of all sources of perturbation, such as particle-wave interactions, it can be seen as a generalization of several diffusion time definitions, such as Chandrasekhar's (1960) one on the two-body relaxation times of stellar systems.

The diffusion timescale, defined as

$$T_D(E) = \overline{E}^2 / D_2(E) \quad (3)$$

for each individual body may thus seem more intuitive. The same definition holds with  $L_z$  to compute  $T_D(L_z)$ .  $E^2(t=0)$  or  $L_z^2(t=0)$  can be used instead of, respectively,  $\overline{E}^2$  or  $\overline{L}_z^2$  without any significant change. The results for all three simulations are displayed in Figures 7 and 8, where the frequency distribution of particles (or mass fraction, as all particles have the same individual mass) is plotted against  $T_D(E)$  and  $T_D(L_z)$ . For the sake of clarity, we have restricted these figures to the range  $10^{-4}$ –90 Gyr, but  $T_D$  can reach much higher values for a few particles.

An obvious outcome is the similarity between the distributions for the three simulations. This form of universality is primarily linked to the similarities of  $D_2(E)$  and  $D_2(L_z)$  distributions for the three simulations. It is also due to the shape of the distribution functions  $DF(E)$  and  $DF(L_z)$  (Figure 3)

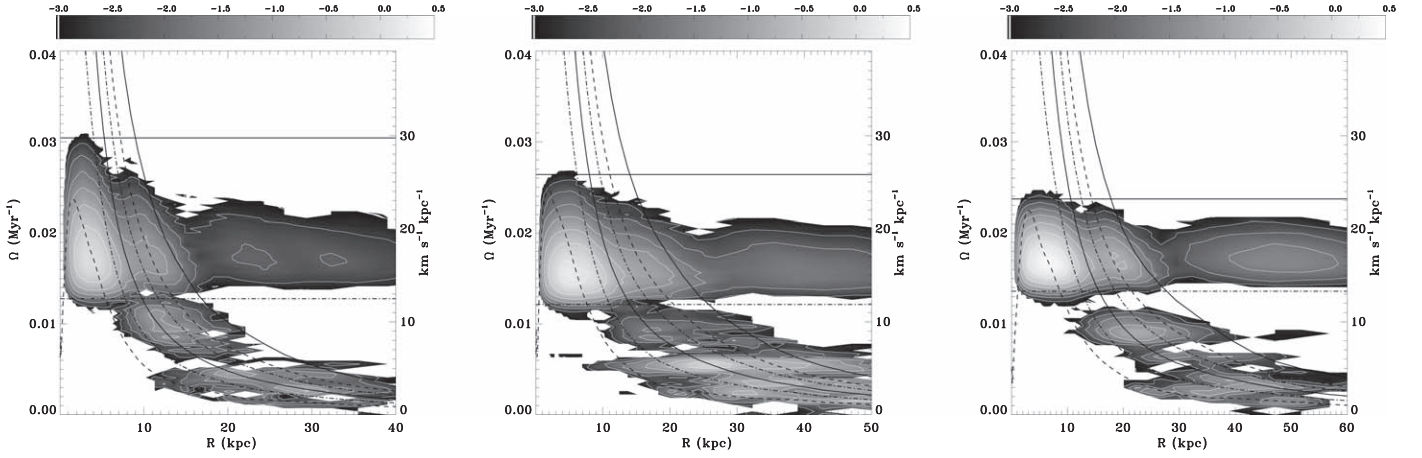


**Figure 5.**  $m = 2$  power spectra in log scale as a function of radius for RunA (left), RunB (middle), and RunC (right) in log scale. The time interval is 2–10 Gyr for RunA and RunB and 3–10 Gyr for RunC. The vertical scales give values of  $\Omega$  in  $\text{Myr}^{-1}$  (left) and in  $\text{km s}^{-1} \text{kpc}^{-1}$  (right). The averaged curves  $\Omega - \kappa/2$  (which allows the ILR to be identified) and  $\Omega + \kappa/2$  (for the OLR) are drawn as black short dashed lines,  $\Omega - \kappa/4$  and  $\Omega + \kappa/4$  (for, respectively, the UHR and 4/1) as dotted-dashed line, and  $\Omega$  as a solid line (for the CR). The horizontal lines represent  $\Omega_p$ , respectively, at the beginning of the time window (full line) and the end (dotted-dashed line).

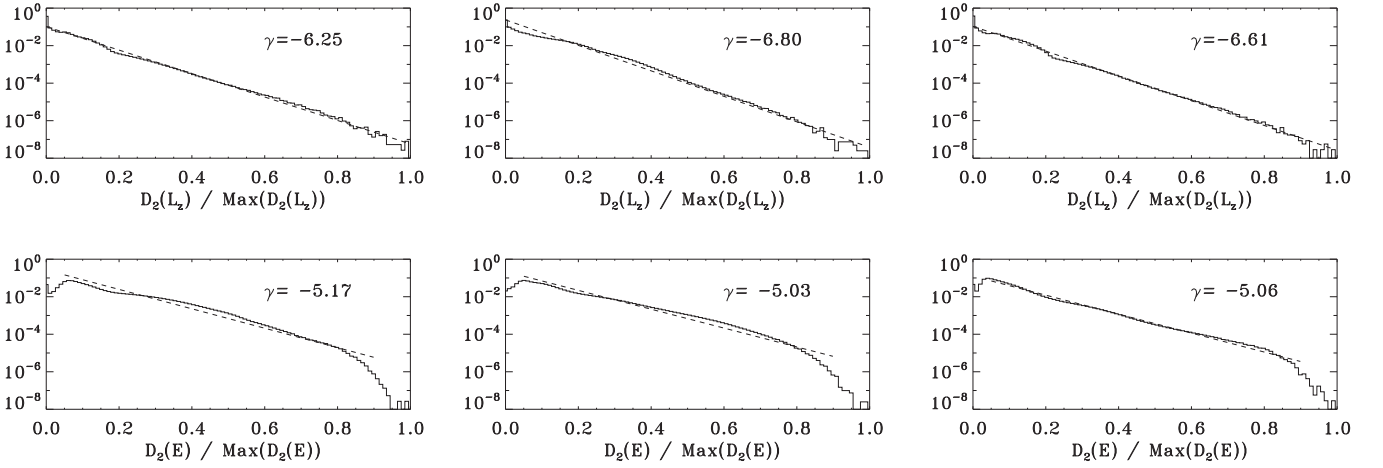


**Figure 6.** Particle number (or mass fraction) as a function of  $D_2(E)$  and  $D_2(L_z)$  for RunA (left), RunB (middle), and RunC (right). For convenience, the number of particles is normalized to  $N_s$  and  $D_2(E)$  and  $D_2(L_z)$  to their respective maxima.  $\gamma$  is the slope fitted by linear regression represented by dashed lines. The extent of the dashed line represents the range over which the fit has been made.

which, although they differ in detail, share the same form. Moreover, it should be stressed here that the timescale chosen is absolute, in Gyr, and not normalized to a maximum as we have done in Figure 6. Timescales are thus quantitatively comparable in terms of values.

### 6.1. E Diffusion Timescale

Dealing first with  $T_D(E)$  distribution only, a first region appears between 0.1 Myr (the minimum time step observed during numerical integration) and a local minimum located at  $\approx 5$  Gyr (RunA),  $\approx 7$  Gyr (RunB), and  $\approx 4$  Gyr (RunC). This time range covers most of the dynamical timescales present in the galaxy’s disk, from its central part to its outermost border. The decrease in mass fraction as a function of  $T_D(E)$  is slower than exponential. This region represents roughly 33% (RunA), 39% (RunB) and 27% (RunC) of the total mass. It is noteworthy that particles with  $T_D(E) \lesssim 0.1$  Myr represent a negligible mass, but  $\approx 35\text{--}42\%$  of the total mass lie in the range  $T_D(E) < 10.54$  Gyr. Apart from the fact that  $T_D(E)$  is calculated on 1 Gyr more for RunA and RunB than for RunC,

we did not find any other simple possible cause that would explain these differences in mass fraction. For instance, we do not see any scaling with the total mass or the initial disk scale length. Differences in the evolution of these three simulations, notably the formation of the bar, the emergence of the spiral arms, etc., are possibly at the origin of these differences in mass fraction.

A second feature, a bump centered at  $\approx 10$  Gyr for RunA and RunB, and  $\approx 8$  Gyr for RunC, might be the footprint of the limited time length of the simulations. On the contrary, no signature due to sampling is detected (i.e., 100 Myr for the calculation of  $D_2$ ).

Finally,  $\approx 58\text{--}65\%$  of particles have  $T_D(E) > 10.54$  Gyr. This means that most of the mass undergoes energy fluctuations that only become significant over times longer than the simulations length, and therefore, in practice, over times that might be greater than the age of the universe.

To understand the properties of the particle populations that contribute to the different timescales, we have plotted in Figure 9  $DF(L_z)$  for various selection of particles made on  $T_D(E)$  for RunC (see Figures 16 and 17 in the Appendix for

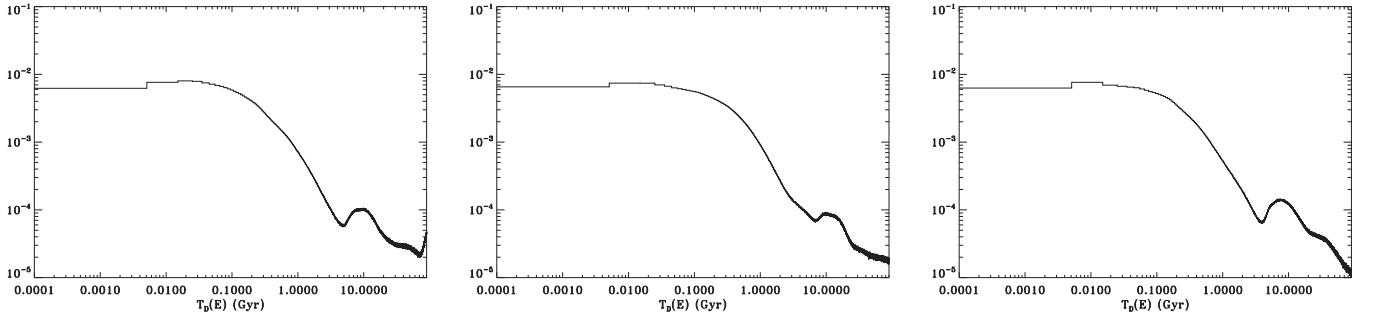


**Figure 7.** Distribution of particle frequency (or mass fraction) as a function of  $T_D(E)$  for RunA (left), RunB (middle) and RunC (right). One particle represents a fraction of  $2.5 \times 10^{-8}$  for RunA and RunC, and  $2.27 \times 10^{-8}$  for RunB. A binsize of 0.01 Gyr has been used.

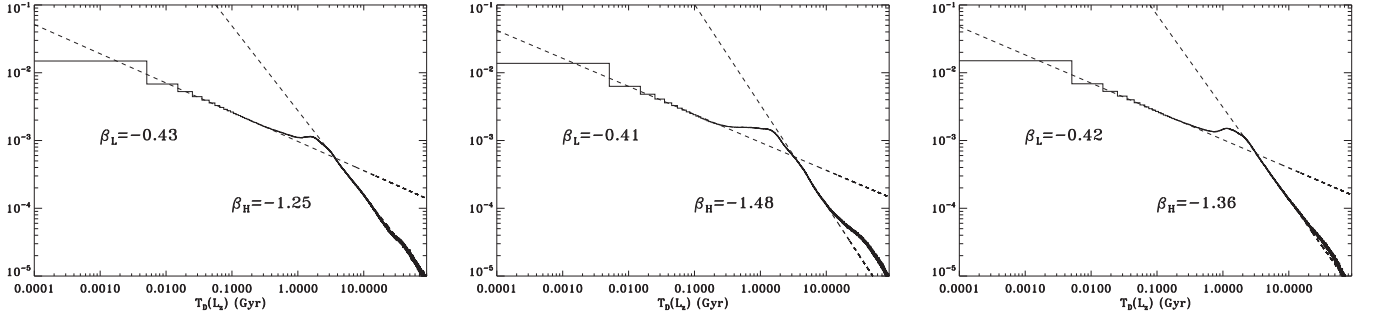


**Figure 8.** Same as Figure 7, but for  $T_D(L_z)$ .

**Table 2**  
Values of the Maxima of  $D_2(E)$  and  $D_2(L_z)$ , and Total Mass

Model	$\max(D_2(E))$ ( $\text{kpc}^4 \text{ Myr}^{-4}$ ) $\text{Myr}^{-1}$	$\max(D_2(L_z))$ ( $\text{kpc}^2 \text{ km}^2 \text{ s}^{-2}$ ) $\text{Myr}^{-1}$	$M_{\text{tot}}$ $M_{\odot}$
RunA	$3.93 \times 10^{-8}$	276.7	$4.2 \times 10^{10}$
RunB	$1.43 \times 10^{-7}$	859.2	$1.2 \times 10^{11}$
RunC	$3.32 \times 10^{-7}$	2292.8	$2.0 \times 10^{11}$
RunC <sup>axi a</sup>	$4.46 \times 10^{-7}$	145.6	$2.0 \times 10^{11}$

**Note.**

<sup>a</sup> See Section 7.

other simulations). The reference time is the origin of the simulation ( $t=0$ ). Particles with  $T_D(E) > 10.54$  Gyr come essentially from populations with  $L_z < 1500 \text{ kpc km s}^{-1}$  (red curve in Figure 9) that are typically well inside the innermost resonances of the bar. For the sake of comparison, an hypothetical circular orbit at the bar ultraharmonic resonance (UHR) at  $t = 3.16$  Gyr has  $L_z \approx 2200 \text{ kpc km s}^{-1}$ . Although the bar is a major gravitational perturbation, which has the ability to cause significant mass redistribution, the fact that resonances isolate the central region from the rest of the galaxy possibly limits the onset of energy diffusion. Therefore, the diffusion timescales in  $E$  are longer than simulation length in the innermost region.

Particles with  $4 < T_D(E) < 10.54$  Gyr (green curve in Figure 9) come from a fraction of the bar population which is close to the corotation barrier. This region contains many bifurcations of orbit families by period doubling (Contopoulos 1983b). An infinite cascade of this type of bifurcation then forms a sequence that leads to stochasticity.

Finally, particles with  $T_D(E) < 4$  Gyr come massively from both the “hot” population and the disk. Their diffusion

timescale is comparable with or shorter than typical dynamical timescales in the disk.

We can therefore summarize the global trend of  $T_D(E)$  by saying that it decreases from the center to the most external regions. This trend will be further discussed in Section 8 and refined.

### 6.2. $L_z$ Diffusion Timescale

Dealing now with  $T_D(L_z)$ , a noteworthy observation is that two slopes appear for  $0.001 \lesssim T_D(L_z) \lesssim 0.3$  Gyr, and  $3 \lesssim T_D(L_z) \lesssim 10$  Gyr in a log–log diagram. These ranges are those on which a line has been fitted by a standard algorithm of linear regression. Therefore, for  $0.001 \lesssim T_D(L_z) \lesssim 0.3$  Gyr,

$$n(T_D) \propto T_D^{\beta_L}, \quad (4)$$

where  $\beta_L \approx -0.42$  in most cases and  $n(T_D)$  is the distribution of particle frequencies (or mass fraction). The second slope with index  $\beta_H$  seems to depend on the simulation parameters.

Below the timescale of 0.3 Gyr, which is also the typical mean bar rotation period for all three simulations, mass is made of particles with low  $L_z$  (Figure 10 for the case of RunC). These particles represent only a small mass fraction, between 8.6% and 9.5%.

On the other side of the distribution, 36%–40% of the mass has  $T_D(L_z) \geq 10.54$  Gyr. All kinds of orbits contribute to this population, but it should be noted that, in the case of RunC, all particles with  $L_z > 3300 \text{ kpc km s}^{-1}$ , i.e., a large fraction of the “hot” population and all disk particles, have very long  $T_D(L_z)$ .

Finally, about half of the mass (51%–54%) has intermediate diffusion times, between 0.3 and 10.54 Gyr. The particles inside the bar form the largest part of this population responsible for the diffusion of the angular momentum. Probably a small fraction of the “hot” population also belongs

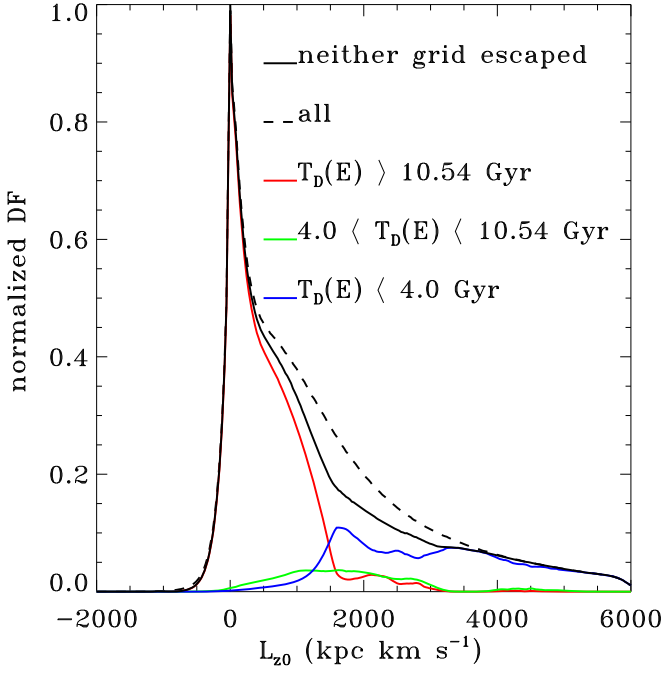


**Figure 9.** Distribution function  $DF(L_z)$  for RunC at  $t=0$ . Dashed line: all particles ( $N_s$ ). Solid line: only particles that neither escaped from the grid and used for  $T_D(E)$  computations. Red line: particles with  $T_D(E) > 10.54$  Gyr. Green line:  $4 < T_D(E) < 10.54$  Gyr. Blue line:  $T_D(E) < 4.0$  Gyr. All DFs have been normalized to  $DF(0)$  with all particles, which is also the maximum.

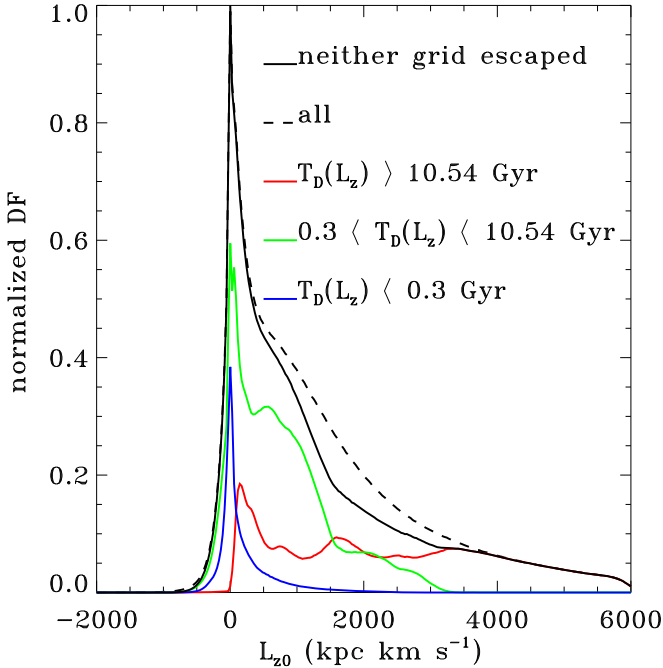


**Figure 10.** Same as Figure 9, but for  $T_D(L_z)$ . The noticeable timescale is now 0.3 Gyr instead of 4 Gyr.

to this category but it is difficult to quantify its contribution more precisely without a detailed orbit analysis that is postponed to a future paper.

In comparison, the global trend of  $T_D(L_z)$  seems to be opposite to that of  $T_D(E)$ : the diffusion timescale increases with the radius.

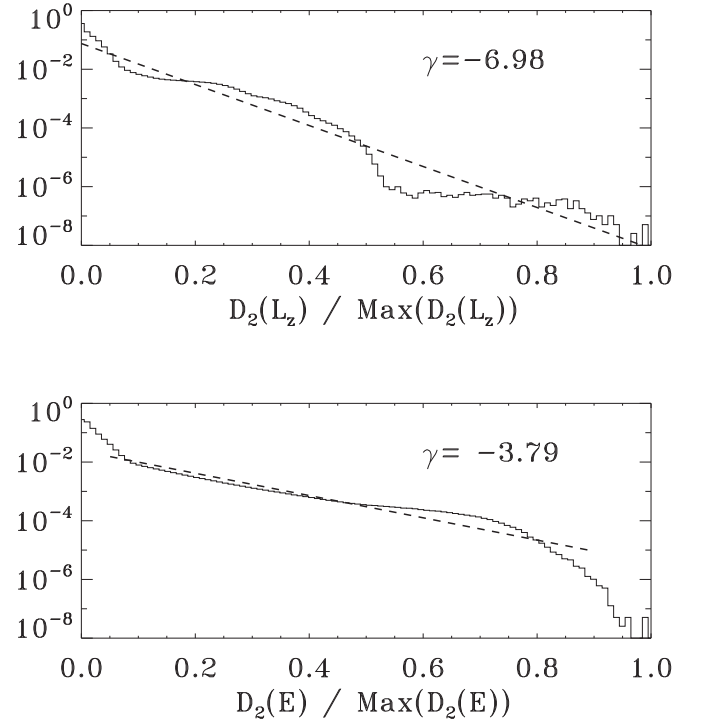


**Figure 11.** Particle number (or mass fraction) as a function of  $D_2(E)$  and  $D_2(L_z)$  for RunC<sup>axi</sup> when the mass density is forced to remain axisymmetric. As for Figure 6, the number of particles is normalized to  $N_s$  and  $D_2(E)$  and  $D_2(L_z)$  to their respective maxima (see the text for values).

## 7. The Axisymmetric Case

An instructive element of comparison is to look at what happens to  $D_2(E)$ ,  $D_2(L_z)$ ,  $T_D(E)$ , and  $T_D(L_z)$  in case a simulation is forced to remain axisymmetric. Both  $E$  and  $L_z$  are now isolating integral of motion. Diffusion rates would be zero if the gravitational potential were due to an infinite number of particles. The potential would then be smooth and stationary. The individual energy of the particles would then be perfectly preserved. Poissonian shot noise due to potential discreteness, forces accuracy and the finite number of particles is however unavoidable. We thus need reference values.

RunC was recalculated by forcing the axisymmetrization of the mass density at each time step, any other parameter being similar to RunC. Let us call it RunC<sup>axi</sup>. The gravitational potential therefore remains close to axisymmetric, no bar or spiral structure can develop. Only axisymmetric waves can propagate in the first Gyr of the simulation, carrying initial angular momentum toward the external regions. For comparison purposes, all rates and timescales were calculated in the same way as RunC, i.e., between  $t = 3.16$  and  $t = 10.54$  Gyr.

Regarding  $D_2(E)$  (Figure 11), even if its maximum ( $4.46 \times 10^{-7}$ ) is close but a little greater than that of RunC (see Table 2), the distribution shape is significantly different. Indeed, a large mass fraction has low values of  $D_2(E)$  (i.e., less than 10% of the maximum). Beyond that, the distribution is flatter than for RunC, which results in a higher  $\gamma$  slope ( $\approx -3.8$  instead of  $\approx -5$ ).

For  $D_2(L_z)$ , not only  $\max(D_2(L_z)) \approx 146$  is much lower than for RunC ( $\approx 2300$ ), and this for the same total mass, but the shape of the distribution is no longer close to a linear relation between the mass fraction and  $D_2/\max(D_2)$ . The scale of  $D_2(L_z)$  has been reduced by a factor of 16. This can be easily

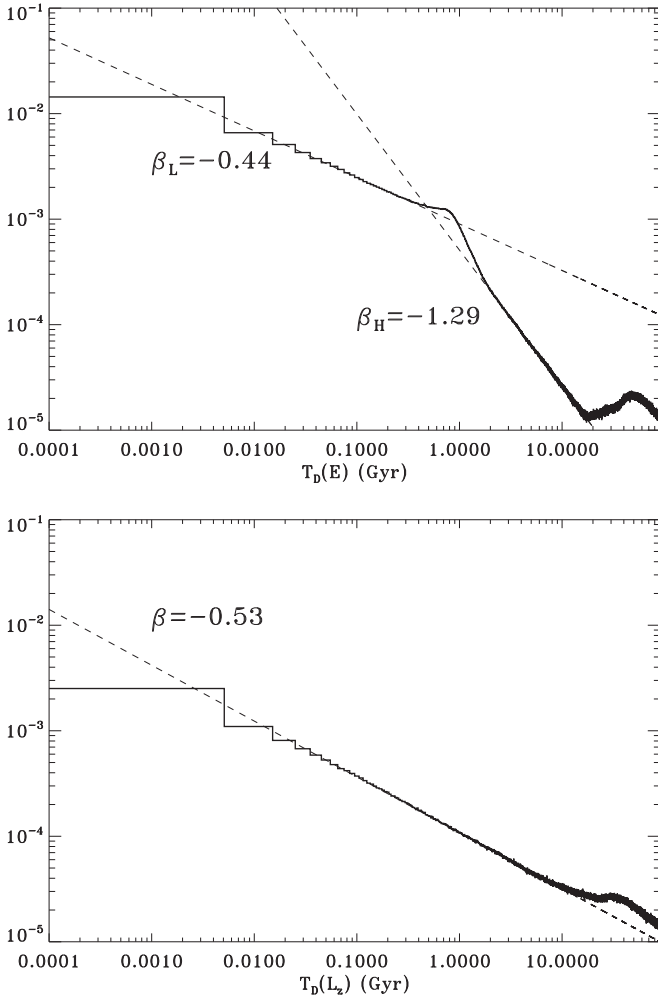


**Figure 12.** Same as Figure 7 (top) and Figure 8 (bottom) for RunC<sup>axi</sup> when the mass density is forced to remain axisymmetric.

understood because a large angular momentum diffusion is not expected in an axisymmetric simulation as  $L_z$  is an integral of motion.

Unexpectedly, the shape of the  $T_D(E)$  distribution (Figure 12 top row) between 0.1 Myr and 4 Gyr is significantly different from those shown in Figure 7. It looks like the  $T_D(L_z)$  distribution for nonaxisymmetric simulations. The two slopes  $\beta_L$  and  $\beta_H$  are moreover similar to those displayed in Figure 8. If we select the particles of RunC<sup>axi</sup> with  $T_D(E) < 2$  Gyr, it appears (Figure 13) that their  $L_z$  corresponds to the so-called “hot” population, although formally this population cannot exist here because the bar and associated resonances are absent. These particles are therefore the ones likely to be most affected by a perturbation, their diffusion time being already the shortest in the axisymmetric case. Particles with  $2 < T_D(E) < 10.54$  Gyr would then be orbits located in the region inside the corotation, where the families of orbits undergo bifurcations. Here again, in the axisymmetric case, and therefore in absence of any pattern frequency, there is no specific resonances.

The  $T_D(L_z)$  distribution of RunC<sup>axi</sup> (Figure 12 bottom row) displays now a unique slope with  $\beta \approx -0.53$  that extends from 0.01 to  $\approx 10$  Gyr. But particles in this range account for only 7% of the total mass compared to more than 50% for the other three nonaxisymmetric simulations. Only orbits with very low  $L_z$  (and thus close to the center) contribute to this region. The rest of the mass (93%) has  $T_D(L_z) \gg 10$  Gyr. This trend is

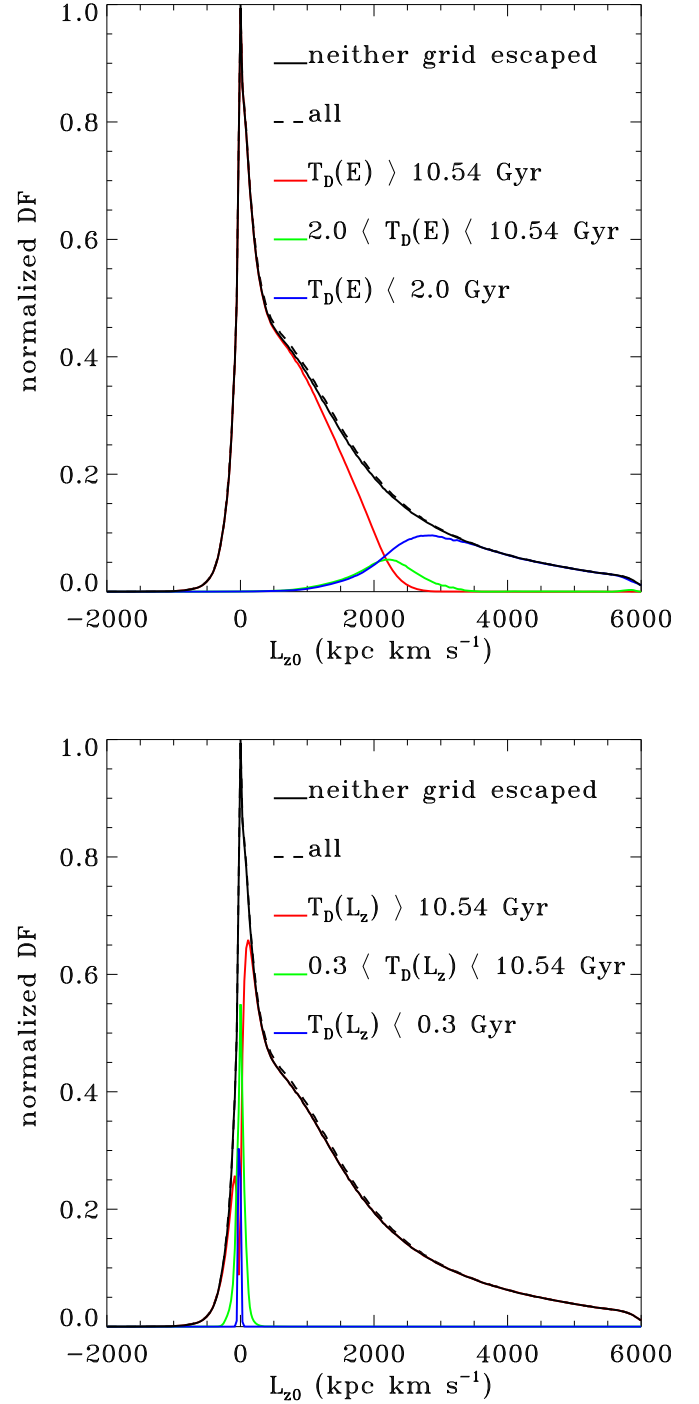


**Figure 13.** Distribution function  $DF(L_z)$  for RunC<sup>axi</sup> at  $t = 0$ . Dashed lines: all particles ( $N_s$ ). Solid lines: only particles that neither escaped from the grid and used for  $T_D(E)$  and  $T_D(L_z)$  computations. Red lines: particles with  $T_D(E)$  or  $T_D(L_z) > 10.54$  Gyr. Green lines:  $2 < T_D(E) < 10.54$  (top) or  $0.3 < T_D(L_z) < 10.54$  Gyr (bottom). Blue lines:  $T_D(E) < 2.0$  Gyr (top) or  $T_D(L_z) < 0.3$  Gyr (bottom). All DFs have been normalized to  $DF(0)$  with all particles, which is also the maximum.

much expected as  $L_z$  is an integral of motion in axisymmetric disks. This illustrates that when a bar, spiral structure, and any other pattern appear in the RunC simulation, these collective oscillations are solely responsible for the diffusion of the angular momentum. As soon as axisymmetry is broken,  $T_D(L_z)$  starts decreasing, leading to  $T_D(L_z) < 10.54$  Gyr for circular orbits with  $L_z < L_z(\text{corotation})$ .

A final observation worth mentioning: the number of escaped particles, defined as those having gone outside the grid even one time step, is only 1.5% for RunC<sup>axi</sup>, compared to 14% for RunC.

## 8. Discussion

### 8.1. Role of Resonances

At resonances, particles can undergo two types of phenomena that are both important for the galactic dynamics. The first one is capture (or trapping) into the resonance. Any particle follows closely an adiabatic trajectory until it crosses a resonant surface. There, the particle trajectory starts following this surface rather than the adiabatic trajectory, causing strong adiabatic invariant (hereinafter referred to as  $I$ ) changes along the exact motion. As the particle may escape from the resonance (after a finite but unpredictable time), it starts following a different adiabatic trajectory with value of  $I$  completely different from the initial one. Initial conditions of particles to be captured and those to cross the resonance without capture are entangled. At the coarse-grained level, this leads to capture probabilities. These capture probabilities are of order of the perturbation strength so that we do not expect a large part of particles to be captured. However, due to the disk rotation, phase trajectories of the averaged system are closed, allowing particles to cross the resonant surface again and again. This significantly increases the probability to be captured on the long term, making resonant capture important for the galactic disk dynamics.

The second phenomenon, scattering, takes place for particles that cross the resonance without capture. The particle trajectory follows closely the adiabatic trajectory, but at the resonant surface it shifts by a very small amount rather than being captured. After crossing the resonance, the particle follows a new adiabatic trajectory, which has moved from a distance of order of the perturbation strength from the original one. The amount by which  $I$  changes depends on the initial conditions. As for capture, multiple scattering is possible and lead to diffusion of the adiabatic invariant on the long term. Therefore, particles passing through resonance change their energy even in absence of trapping. However, if the resonant system contains a separatrix, the mean energy change due to scattering is finite. Multiple scatterings lead to either acceleration or deceleration of particles. In absence of such a separatrix, the energy change over multiple scatterings is diffusive.

In the context of epicyclic approximation, localizing resonances requires the computation of the circular orbit frequency  $\Omega$  and the radial epicyclic frequency  $\kappa$ . Strictly speaking, these frequencies predict the oscillation frequencies of the orbits in the axisymmetrical case limits only. They do not provide any indication of whether families of periodic orbits do follow such oscillations when the bar growth breaks the axisymmetry. However, a number of previous orbital studies (see Michel-Dansac & Wozniak 2006, and discussion therein) suggest that the epicyclic approximation could lead to an acceptable estimation of the resonance locations, in particular if we are mainly interested in their evolution rather than their accurate absolute position. For instance, using a careful integration of orbits to compute  $\Omega$  and  $\kappa$ , Michel-Dansac & Wozniak (2006) found that the error on the corotation radius remains within 10%.

In the case of barred galaxies, the resonant area is a large region around the idealized corotation radius, in the sense of a radial solution of the equation  $\Omega(R_{\text{cor}}) = \Omega_p$  as defined by the linear theory of resonances. Indeed, Lagrangian points are defined as being the points of equilibrium between centrifugal and centripetal forces along the main axis of the bar perturbation. The radii of these points converge toward the corotation circle when the bar perturbation vanishes.  $L_{1,2}$  and  $L_{4,5}$  are the radii of the Lagrangian points along respectively the major-axis and intermediate axis (minor-axis in a face-on projection) of the bar perturbation. Michel-Dansac & Wozniak (2006) have shown that the relative amplitude of the difference between  $L_{1,2}$  and  $L_{4,5}$  rarely exceeds 15% even in very strong bar phases. A standard value for a slowly evolving bar seems to be in the range 5%–10%. Moreover, the amplitude of the difference between  $L_{1,2}$  and  $L_{4,5}$  is roughly proportional to the bar strength. When the bar gets stronger, the difference between  $L_{1,2}$  and  $L_{4,5}$  increases,  $L_{4,5}$  being always smaller than  $L_{1,2}$ . Therefore, the corotation radius always lies between the Lagrangian points radii but is closer to  $L_{1,2}$  than  $L_{4,5}$ . Thus, when the corotation is mentioned, the region concerned is an oval ring whose width depends on the strength of the bar. Ceverino & Klypin (2007) focused on the action of the bar in the redistribution of  $L_z$  and, in particular, the capture of particles by corotation. Their work clearly shows that the scope of the action of the bar goes well beyond corotation. In particular, they show how strong the variations of  $L_z$  of the particles trapped around stable Lagrange points are.

It is moreover well established that a rotating stellar bar transports angular momentum outwards, resulting in a decrease in  $\Omega_p$ . This decrease is almost linear with time in absence of a dissipative component (gas) and any star formation. For instance, this is the case of the three  $N$ -body simulations described in Section 4. As a result, the corotation radius increases over time, as do other resonance radii. It is the whole resonance system that moves, whether it is the one generated by the bar or by any other structure likely to lose/gain angular momentum.

In Figure 14 we have displayed diffusion timescales  $T_D(E)$  and  $T_D(L_z)$  averaged over sets of particles sampled by  $\overline{L_z}$  ranges, for the case of RunC.  $\overline{L_z}$  is now time-averaged over  $\approx 7$  Gyr. It is here a proxy for the mean radial position of particles. In this  $\langle T_D \rangle - \overline{L_z}$  plot, we can overlay the approximate position of bar resonances determined in the linear epicyclic approximation. As the entire resonance system moves outwards during the evolution of the galaxy, we have plotted the position of the UHR at  $t = 3.16$  Gyr and the OLR at  $t = 10.54$  Gyr. This delimits the range in  $L_z$  occupied by all bar resonances during the evolution. The specific range covered by the corotation is approximately represented by the shaded area but can be more extended when  $L_{1,2}$  and  $L_{4,5}$  positions are considered.

This averaged view of timescales and angular momentum confirms the statements made in Section 6. On average,  $\langle T_D(E) \rangle$  decreases from the center to the outermost regions. In the range of  $\overline{L_z}$  delimited by resonances positions,  $\langle T_D(E) \rangle$  remains below 1 Gyr, and goes down to 0.1 Gyr. Typical  $\langle T_D(E) \rangle$  values outside OLR remain of the order of the Gyr or below.

In contrast to  $\langle T_D(E) \rangle$ ,  $\langle T_D(L_z) \rangle$  increases from the center outwards. In the bar resonance region, it reaches values much higher than 10 Gyr. The diffusion of  $L_z$  is therefore more effective well inside the UHR. To avoid any misunderstanding,

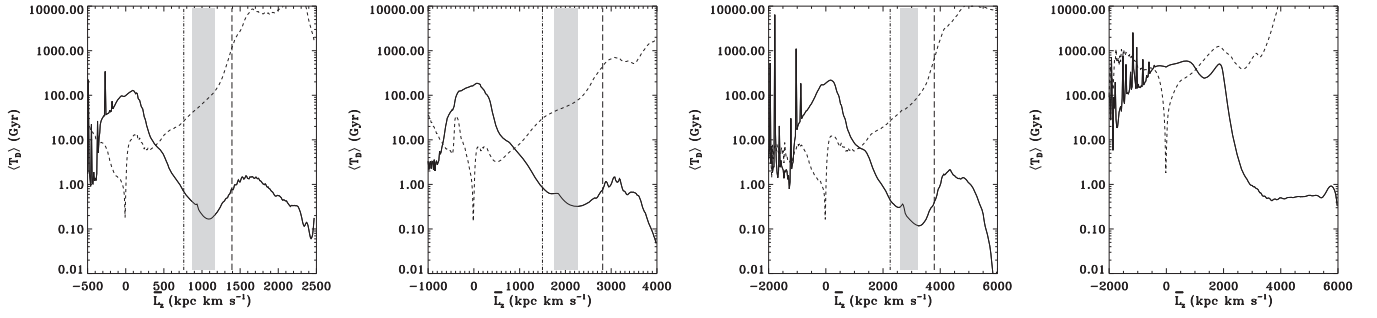


**Figure 14.**  $\langle T_D(E) \rangle$  (full line) and  $\langle T_D(L_z) \rangle$  (dashed line) as a function of  $L_z$  for RunA, RunB, RunC, and RunC<sup>ax1</sup> from left to right. The shaded area delimits the region occupied by bar corotation during the 6 (RunA and RunB) and 7 Gyr (RunC) evolution. Vertical lines show  $L_z$  for the innermost bar UHR (dotted-dashed) and the outermost OLR (long-dashed) positions reached.

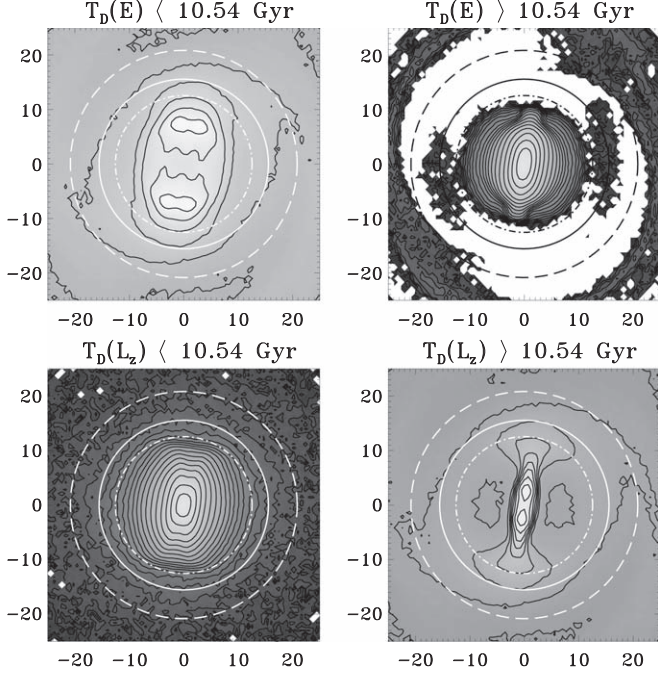


**Figure 15.** Projection of mass distribution on  $x$ - $y$  plane for particles selected according to  $T_D(E)$  (top) and  $T_D(L_z)$  (bottom) for RunC at  $t = 10.54$  Gyr. The log grayscale is identical for all four figures. Contour labels are spaced by 0.25 dex. The white or black circles show the position for the innermost UHR (dotted-dashed), the corotation (full line), and the outermost OLR (long-dashed). Spatial scale is in kpc.

we remind here that we only study the phase after the formation of the bar ( $t > 3$  Gyr), in a regime that can be considered as quiet.

There have been some debates on the action of the OLR as a barrier to stellar migration (Halle et al. 2015; Monari et al. 2016). In the case of our simulations,  $\langle T_D(E) \rangle$  does indeed show a bump just after the OLR but the characteristic timescale remains of the Gyr order.  $\langle T_D(L_z) \rangle$  continues to increase well beyond the bar OLR, even for RunC<sup>ax1</sup>. Therefore, we cannot confirm a specific signature of a barrier due to the bar OLR.

Formally,  $L_z$  is a good proxy for the radius only for orbits close to circular. To verify the true spatial distribution, the mass distribution obtained for short and long diffusion times (arbitrarily defined as shorter or longer than the simulation length) can be projected. Figure 15 shows the mass projected in the  $x$ - $y$  plane for  $T_D$  less than or greater than 10.54 Gyr. It globally confirms the analysis of Section 6 but suggests that a more detailed analysis must be performed. A few features

deserve to be mentioned. Particles with  $T_D(E) > 10.54$  Gyr includes a population that might be trapped around  $L_{4,5}$  Lagrangian points. They also included stable  $x_1$  orbits inside the UHR, where their shape is purely elliptical (Contopoulos 1983a). Beyond the UHR bifurcation,  $x_1$  orbits become rectangular-like, develop loops, and can become unstable. Their contribution is visible in the mass distribution for  $T_D(E) < 10.54$  Gyr. A much more detailed study of the  $T_D$  spatial distribution, and its relation to orbits families, is postponed to a dedicated future paper.

## 8.2. Stochastic Diffusion

Results similar to Brunetti et al. (2011) have been reached: the role of the “hot” population is highlighted in both studies and the diffusion timescale depends on the radial position. However, a quantitative comparison with Brunetti et al. (2011) is not straightforward. The definition of their diffusion coefficient is different and they expressed it as a function of time and radius. Their study is based on Fourier’s law of heat conduction. Heat conduction is a non-equilibrium phenomenon. A coarse-grained description of the phenomenon with a clear separation between microscopic and macroscopic scales can be assumed. At the microscopic scale, heat carriers which are molecules and atoms in gas and liquids, phonons in solids, evolve as a result of a deterministic Hamiltonian description, whereas at macroscopic scale phenomenological Fourier’s law implies a diffusive transfer of energy. However a rigorous derivation of this law starting from a microscopic Hamiltonian description is still lacking (Dhar 2008).

Microscopically we have to think about heat carriers colliding randomly and the result is a heat diffusion. However, in a pure stellar  $N$ -body system, hard collisions are rare. Encounters are the dominant process, especially weak ones, which makes the Fokker–Planck equation the traditional tool for the study of stellar systems through the frictional and diffusion coefficients (Lichtenberg & Lieberman 1992; Binney & Tremaine 2008).

It can be shown that a DF whose evolution over time is governed by the Fokker–Planck equation also follows a diffusion equation of Fourier’s form, with the same diffusion coefficient, provided that a relationship with the friction coefficient is respected (see Lichtenberg & Lieberman 1992). Therefore, the formalism used by Brunetti et al. (2011) may be similar to that of Fokker–Planck.

For simple Hamiltonians, a generalized Fokker–Planck equation can be derived to include the energy drift due to scattering and fast transport in phase space due to trapping/escape. This derivation goes beyond the purpose of this paper.

The Chirikov coefficient implicitly includes all effects due to resonances, and resonances overlaps due to several forcing patterns, as well as effects due to a noisy potential.

### 8.3. Limitations

For our first paper on this topic, we have decided to restrict the exploration of  $E$  and  $L_z$  variations to the simplest type of simulations, the pure  $N$ -body case. Indeed, the absence of a gaseous component is a major main limitation that has several clear consequences. Without gas, there is no possibility to form a new population whose kinematics might cool down the disk (Wozniak 2015, for instance). Another missing fluid is dark matter. The main effect of a live dark halo (except to flatten the rotation curve of the disk at a large distance) is to permit the exchange of angular momentum with the stellar disk. The rate and the amplitude of these exchanges depend on the velocity dispersion of both the disk and the halo, and on the relative halo mass. Depending on the rate at which the stellar disk loses its angular momentum, the bar grows quite differently. Considering Martinez-Valpuesta et al. (2006) simulations as representative, roughly  $2/3$  of the angular momentum loses by the bar-unstable part of the stellar disk is absorbed by the halo, the rest going to the outer disk. Most of these exchanges happen during the buckling of the bar, which, in the case of our simulations, occurs for  $t < 3$  Gyr.

A final limitation comes from the genuine nature of galaxies, which are much more complex than these idealized simulations. Much of this complexity comes from perturbations by random sources. These sources can be intrinsic (such as molecular clouds or Poissonian shot noise) or extrinsic (satellites accretion, globular clusters, etc.). All these perturbations could contribute to reduce diffusion times, but this remains to be demonstrated in the specific case at hand.

## 9. Conclusions

We have computed Chirikov (1979) diffusion rates ( $D_2(E)$  and  $D_2(L_z)$ ) and related diffusion timescales ( $T_D(E)$  and  $T_D(L_z)$ ) for energy ( $E$ ) and angular momentum ( $L_z$ ) in pure  $N$ -body simulations of disk galaxies developing bars and spiral structures. These quantities were only calculated once the bar was perfectly settled in order to reflect the evolution of the disk under the effect of its presence.

We summarize our results as follows:

1. Both  $E$  and  $L_z$  diffuse during the evolution of a stellar disk, under the effect of intrinsic perturbations caused by the bar and spiral structures. In particular, bars and spiral

structures are responsible for shortening diffusion timescales.

2. Diffusion timescales are shorter than the simulations length (i.e.,  $\approx 10$  Gyr) for different particle populations depending on whether the diffusion of  $E$  or  $L_z$  is considered. Consequently, the regions affected by the diffusion differ according to the quantity that diffuses.
3. The distribution function of Chirikov diffusion rates  $D_2$  has the same shape regardless the simulation considered. It can be approximate by the equation  $\log n(D_2) \propto \gamma D_2 / \max(D_2)$  where  $\gamma \approx -5.0$  for  $D_2(E)$  and  $\gamma$  is in the range  $[-6.61; -6.21]$  for  $D_2(L_z)$ .
4. At first order, values of  $D_2(E)$  remain within the same range in axisymmetric and nonaxisymmetric simulations unlike for  $D_2(L_z)$ .
5.  $T_D(E)$  is shorter than simulation length for particles belonging to the “hot” population, the disk, and families of orbits lying between the bar UHR and corotation. It is minimal (and shorter than 1 Gyr) in the region delimited by the set of bar resonances (between UHR and OLR).
6.  $T_D(L_z)$  is shorter than simulation length mainly for particles inside the bar region (i.e., inside the UHR).
7. On average,  $T_D(L_z)$  increases with radius while  $T_D(E)$  tends to decrease from the center to the most external regions.
8. The so-called “hot” population, which navigates between the bar and the disk, plays only an important role in diffusion of  $E$ .

This article is limited to a first exploration of the results obtained with the Chirikov diffusion rate. Next articles will explore in greater depth the phenomena of migration, diffusion and resonance, particularly in terms of orbital structure.

First, I thank the referee for the very constructive comments. I acknowledge the University of Strasbourg HPC department and the Meso@LR computing center of the University of Montpellier for providing access to computing resources. Part of the computing resources were funded by grants from the IDEX Unistra and the Scientific Council of the University of Montpellier.

## Appendix

In this appendix, we show the equivalent of Figures 9 and 10 for runs A and B (see Figures 16 and 17). The conclusions are similar to those in Section 6.

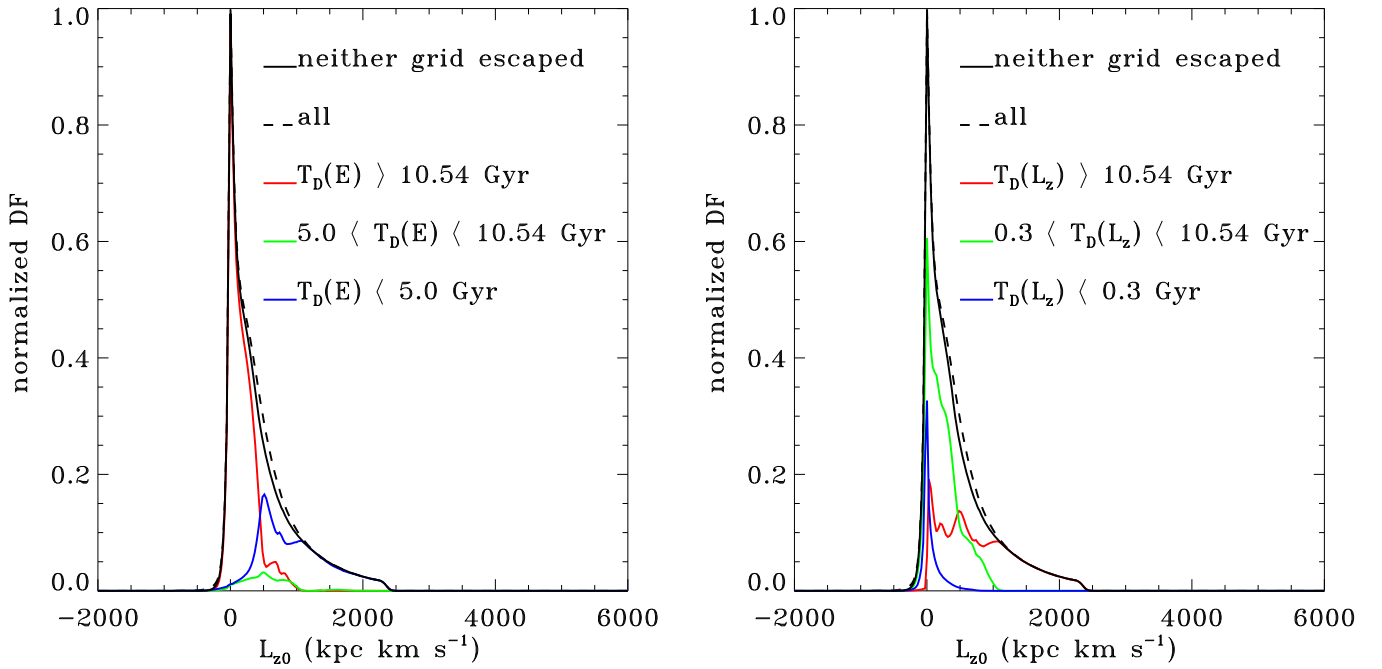


**Figure 16.** Top row: distribution function  $DF(L_z)$  for RunA at  $t = 0$ . Dashed line: all particles ( $N_s$ ). Solid line: only particles that neither escaped from the grid and used for  $T_D(E)$  computations. Red line: particles with  $T_D(E) > 10.54$  Gyr. Green line:  $T_D(E) > 4.0$  Gyr. Blue line:  $T_D(E) < 4.0$  Gyr. All DFs have been normalized to  $DF(0)$  with all particles, which is also the maximum. Bottom row: same as top row, but for  $T_D(L_z)$ . The noticeable timescale is now 0.3 Gyr instead of 4 Gyr.

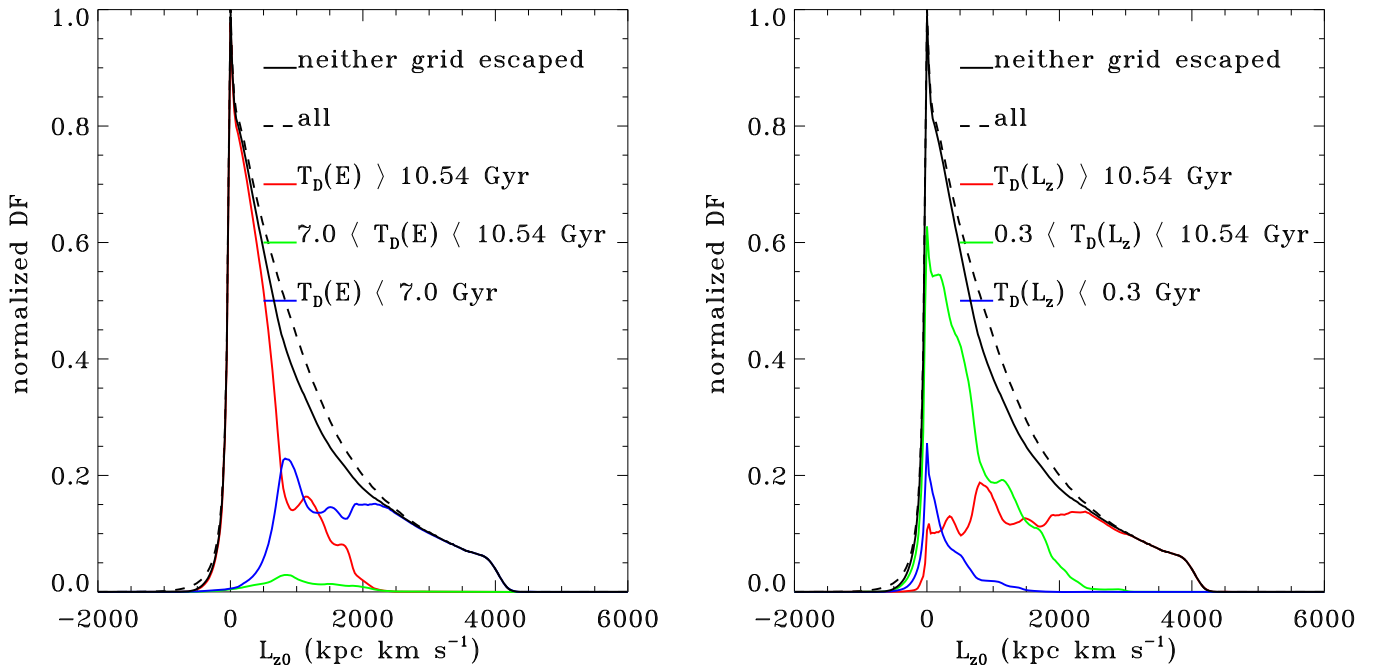


**Figure 17.** Top row: distribution function  $DF(L_z)$  for RunB at  $t = 0$ . Dashed line: all particles ( $N_s$ ). Solid line: only particles that neither escaped from the grid and used for  $T_D(E)$  computations. Red line: particles with  $T_D(E) > 10.54$  Gyr. Green line:  $T_D(E) > 4.0$  Gyr. Blue line:  $T_D(E) < 4.0$  Gyr. All DFs have been normalized to  $DF(0)$  with all particles, which is also the maximum. Bottom row: same as top row, but for  $T_D(L_z)$ . The noticeable timescale is now 0.3 Gyr instead of 4 Gyr.

### ORCID iDs

Hervé Wozniak  <https://orcid.org/0000-0001-5691-247X>

### References

Binney, J., & Tremaine, S. 2008, *Galactic Dynamics* (2nd ed.; Princeton, NJ: Princeton Univ. Press)  
 Brunetti, M., Chiappini, C., & Pfenniger, D. 2011, *A&A*, **534**, A75  
 Buder, S., Lind, K., Ness, M. K., et al. 2019, *A&A*, **624**, A19

Ceverino, D., & Klypin, A. 2007, *MNRAS*, **379**, 1155  
 Chandrasekhar, S. 1960, *Principles of Stellar Dynamics* (New York: Dover)  
 Chirikov, B. V. 1979, *PhR*, **52**, 263  
 Contopoulos, G. 1983a, *A&A*, **117**, 89  
 Contopoulos, G. 1983b, *ApJ*, **275**, 511  
 Dhar, A. 2008, *AdPhy*, **57**, 457  
 Edvardsson, B., Andersen, J., Gustafsson, B., et al. 1993, *A&A*, **275**, 101  
 Halle, A., Di Matteo, P., Haywood, M., & Combes, F. 2015, *A&A*, **578**, A58  
 Haywood, M. 2008, *MNRAS*, **388**, 1175  
 Hernquist, L. 1993, *ApJS*, **86**, 389

- Lichtenberg, A., & Lieberman, M. 1992, *Regular and Chaotic Dynamics* (New York: Springer)
- Mackereth, J. T., Bovy, J., Leung, H. W., et al. 2019, *MNRAS*, **489**, 176
- Martinez-Valpuesta, I., Shlosman, I., & Heller, C. 2006, *ApJ*, **637**, 214
- Michel-Dansac, L., & Wozniak, H. 2006, *A&A*, **452**, 97
- Minchev, I., & Famaey, B. 2010, *ApJ*, **722**, 112
- Minchev, I., Famaey, B., Combes, F., et al. 2011, *A&A*, **527**, A147
- Miyamoto, M., & Nagai, R. 1975, *PASJ*, **27**, 533
- Monari, G., Famaey, B., Siebert, A., et al. 2016, *MNRAS*, **461**, 3835
- Pfenniger, D., & Friedli, D. 1991, *A&A*, **252**, 75
- Pfenniger, D., & Friedli, D. 1993, *A&A*, **270**, 561
- Roškar, R., Debattista, V. P., Quinn, T. R., & Wadsley, J. 2012, *MNRAS*, **426**, 2089
- Sellwood, J. A., & Binney, J. J. 2002, *MNRAS*, **336**, 785
- Soubiran, C., Bienaymé, O., Mishenina, T. V., & Kovtyukh, V. V. 2008, *A&A*, **480**, 91
- Sparke, L. S., & Sellwood, J. A. 1987, *MNRAS*, **225**, 653
- Wielen, R. 1977, *A&A*, **60**, 263
- Wozniak, H. 2015, *A&A*, **575**, A7
- Wozniak, H., & Pfenniger, D. 1997, *A&A*, **317**, 14
- Wozniak, H., & Pfenniger, D. 1999, *CeMDA*, **73**, 149
- Zang, T. A., & Hohl, F. 1978, *ApJ*, **226**, 521